Quarterly Technical Report

Defects and Impurities in 4H- and 6H-SiC Homoepitaxial Layers: Identification, Origin, Effect on Properties of Ohmic Contacts and Insulating Layers and Reduction

Supported under Grant #N00014-95-1-1080
Office of the Chief of Naval Research
Report for the period 1/1/97-3/31/97

R. F. Davis, M. O. Aboelfotoh, B. J. Baliga*, R. J. Nemanich†,
R. S. Busby†, S. W. King, M. L. O'Brien†,
Department of Materials Science and Engineering
*Department of Electrical and Computer Engineering
†Department of Physics
North Carolina State University
Campus Box 7907
Raleigh, NC 27695-7907

March, 1997

REPORT DOCUMENTATION PAGE

Form Approved
OMB No. 0704-0188

1. AGENCY USE ONLY *(Leave blank)*	2. REPORT DATE	3. REPORT TYPE AND DATES COVERED
	March, 1997	Quarterly Technical 1/1/97–3/31/97

4. TITLE AND SUBTITLE
Defects and Impurities in 4H- and 6H-SiC Homoepitaxial Layers: Identification, Origin, Effect on Properties of Ohmic Contacts and Insulating Layers and Reduction

5. FUNDING NUMBERS
ydl495l---01
312
N00179
N66020
4B855

6. AUTHOR(S)
R. F. Davis, M. O. Aboelfotoh, B. J. Baliga and R. J. Nemanich

7. PERFORMING ORGANIZATION NAME(S) AND ADDRESS(ES)
North Carolina State University
Hillsborough Street
Raleigh, NC 27695

8. PERFORMING ORGANIZATION REPORT NUMBER
N00014-95-l-1080

9. SPONSORING/MONITORING AGENCY NAMES(S) AND ADDRESS(ES)
Sponsoring: ONR, Code 312, 800 N. Quincy, Arlington, VA 22217-5660
Monitoring: Administrative Contracting Officer, Regional Office Atlanta
Regional Office Atlanta, 101 Marietta Tower, Suite 2805
101 Marietta Street
Atlanta, GA 30323-0008

10. SPONSORING/MONITORING AGENCY REPORT NUMBER

11. SUPPLEMENTARY NOTES

12a. DISTRIBUTION/AVAILABILITY STATEMENT
Approved for Public Release; Distribution Unlimited

12b. DISTRIBUTION CODE

13. ABSTRACT ***(Maximum 200 words)***

Exposure of the 6H-SiC(0001)$_{Si}$ surface to atomic H selectively removed Si and converted the (3×3) surface to a (1×1) surface as determined from the results of X-ray photoelectron spectroscopy (XPS), Auger electron spectroscopy (AES), low energy electron diffraction (LEED), and temperature programmed desorption (TPD). Reduction and loss of the Si 2p XPS peak from the (3×3) surface were observed. A three-step oxide growth process is being developed. The system will allow for an integrated process to be used in the investigation of oxide growth on 6H- and 4H-SiC. Preliminary investigations of the surface preparation revealed that SiC is not as readily cleaned as Si.

14. SUBJECT TERMS
4H-SiC, 6H-SiC, surface preparation, cleaning, UV/O_3, oxidation, carbidic C, XPS, x-ray photoelectron spectroscopy, Auger electron spectroscopy, AES, low energy electron diffraction, LEED, silicon carbide, x-ray photoelectron diffraction, XPD, oxide

15. NUMBER OF PAGES
30

16. PRICE CODE

17. SECURITY CLASSIFICATION OF REPORT	18. SECURITY CLASSIFICATION OF THIS PAGE	19. SECURITY CLASSIFICATION OF ABSTRACT	20. LIMITATION OF ABSTRACT
UNCLAS	UNCLAS	UNCLAS	SAR

Table of Contents

I. Introduction

The two most important materials-related problems affecting the performance of all SiC devices and their associated components (e.g., contacts) are the defects and the undesired impurities which become incorporated in the homoepitaxial SiC layers in which all devices are currently fabricated. Bhatnagar [1] has shown that the reverse blocking leakage current in high voltage Schottky diodes is three orders of magnitude higher than theoretically predicted as a result of defects in the epi-layer. The formation of micropipes, stepped screw dislocations, interacting dislocation loops, polyganized networks of dislocations and growth twins as well as stacking faults during the sublimation growth of SiC boules are likely the root cause of some of the defects in the epitaxial layer. However, with the exception of the micropipes, the types and concentrations of line, planar and other three-dimensional defects and their effect on the performance of devices and individual device components in the important epi-layer have not been similarly determined. As such, it is not known which of the latter defects actually are translated from the wafer into the epi-layer during its deposition and, therefore, should be vigorously controlled during boule growth and which defects are generated during deposition.

The relatively uncontrolled occurrence of the n-type donor of N and deep level compensating impurities such as Ti in the epilayer have been identified via secondary ion mass spectrometry, photoluminescence and cathodoluminescence investigations. However, the origins of essentially all of these impurities are unknown. For high-temperature, -power and -frequency devices, it is highly desirable to control or eliminate these impurities such as to attain undoped films with uncompensated carrier concentrations of 10^{14} cm^{-3}—two orders of magnitude lower than what is, at present, normally achieved in standard commercial depositions.

The formation of low resistivity and thermally stable ohmic contacts to 4H- and 6H-SiC remains a serious problem in the development of SiC device technology. For SiC power devices to have an advantage over Si, the contact resistivities must be below 1×10^{-5} W-cm^2, as noted by Alok, *et al.* [2]. In addition, the electrical characterization of state-of-the-art SiC films depends on the ability to fabricate ohmic contacts on material with low carrier concentrations. Therefore, better ohmic contacts are needed both for improving device performance and for improving the quality of films which can be grown. The thermal stability of ohmic contacts is of particular concern for p-type SiC, which have traditionally relied on low melting point Al or Al alloys to dope the SiC surface below the contacts. These materials are not suitable for devices intended for high-temperature operation. While the fabrication of ohmic contacts to SiC has also normally depended on the attainment of a very heavily-doped near-surface region, the introduction during deposition of high levels of dopants in the near surface device region of the epi-layer prior to the deposition of the contact or by ion implantation through the contact makes probable the introduction of point and line defects as a result of the induced strain in the lattice.

Based on all of these issues and recent experiments already performed at NCSU, our goals are to produce contacts which are thermally stable and have low contact resistivities while also reducing the need for doping by ion implantation.

To fabricate most microelectronic devices, the growth or deposition of stable insulators is needed to provide both passivating layers and gate dielectrics. Silicon carbide is almost invariably thermally oxidized, albeit at a slower rate, in the same manner and temperature range that is employed for Si. Most of the previous studies regarding the oxidation of SiC have been concerned with polycrystalline materials. It has been shown by Harris and Call [3] and Suzuki, *et al.* [4] that the (0001) face of 6H-SiC oxidizes according to the same linear-parabolic equation reported for Si by Deal and Grove [5]. The model states that the initial stage of oxidation is reaction rate limited and linear, but becomes parabolic as the diffusion of the oxidant through the oxide becomes the rate limiting factor. Research at NCSU by Palmour, *et al.* [6] has demonstrated that the oxidation process on SiC in wet and dry oxygen and wet argon obeys the linear-parabolic law. Both wet processes had a slower rate than dry oxidation at 1050°C and below. The dry oxides exhibited a very flat surface; in contrast, SEM and TEM revealed that wet oxidation preferentially oxidizes dislocation bands, causing raised lines on the oxide and corresponding grooves in the SiC. It was proposed that the much higher solubility of H_2O in SiO_2 as compared to that of O_2 allows wet oxidation to be preferential.

All of the oxidation studies on all polytypes of semiconductor quality SiC have been conducted on n-type material with the exception of the investigation by Palmour *et al.* [6]. The objective of this study was the determination of the redistribution of the common electrical dopants of N, P, Al and B during thermal oxidation of SiC films at 1200°C in dry O_2. Experimental segregation coefficients and interfacial concentration ratios were determined. Secondary ion mass spectrometry revealed that B and Al depleted from the SiC into the growing oxide while N and P were found to pile up in the SiC as a result of the loss of the SiC to the oxide formation. Aluminum is now used almost universally as the p-type dopant in SiC. The electrical properties of oxides thermally grown on n-type SiC normally have reasonably favorable characteristics of high breakdown voltage and low leakage currents. However, the reverse is true for thermally grown oxides on p-type SiC, as shown by Baliga and his students at NCSU. It is believed that at least two of the causes of the poor performance on a p-type material are the existence of the Al in the oxide and at the oxide/SiC interface and the dangling oxygen bonds which this species creates in the oxide as a result of a difference in oxidation state (+3) compared to that of Si (+4) and the existence of C at the SiC/insulator interface. Methods of effectively cleaning SiC surfaces prior to oxidation to deposit and grow oxides on p-type material under UHV conditions and determine the effect of Al redistribution and C concentrations at the interface on the properties of the oxide must be determined. In addition,

the effect of existing line and planar defects in the SiC epi-layer on the properties of the thermally grown and deposited oxide must be ascertained.

The research conducted in this reporting period and described in the following sections has been concerned with (1) the X-ray photoelectron diffraction from (3×3) and ($\sqrt{3}\times\sqrt{3}$)R30° 6H-SiC(0001)$_{Si}$, surfaces and (2) the development and use of a system for integrated surface cleaning and oxide formation on 6H-SiC. The following individual sections detail the procedures, results, discussions of these results, conclusions and plans for future research. Each subsection is self-contained with its own figures, tables and references.

References

1. M. Bhatnagar, Ph. D. Thesis, North Carolina State University, 1994.
2. D. Alok, B. J. Baliga and P. K. McLarty, IEDM Technical Digest, IEDM 1993, 69 (1993).
3. R. C. A. Harris and R. L. Call in *Silicon Carbide–1973*, R. C. Marshall, J. W. Faust and C. E. Ryan, Eds. University of South Carolina Press, Columbia, S. C., 1974, p. 534.
4. Suzuki, *et al.*, Jap. Journ. Appl. Phys. **21**, 579 (1982).
5. B. E. Deal and A. S. Grove, J. Appl. Phys. **36**, 3770 (1965).
6. J. W. Palmour, R. F. Davis, H. S. Kong, S. F. Corcoran and D. P. Griffis, J. Electrochem. Soc. **136**, 502 (1989).

II. X-ray Photoelectron Diffraction from (3×3) and ($\sqrt{3}\times\sqrt{3}$)R3° $(0001)_{Si}$ 6H-SiC Surfaces

Sean W. King, *Richard S. Busby, *Robert J. Nemanich, and Robert F. Davis, Department of Materials Science and Engineering, *Department of Physics, North Carolina State University, Raleigh, NC 27695

Abstract

High resolution (±1°) x-ray photoelectron diffraction (XPD) patterns were obtained along high symmetry azimuths of (3×3) and ($\sqrt{3}\times\sqrt{3}$)R30° reconstructed $(0001)_{Si}$ 6H-SiC surfaces. The data obtained were compared to previously reported XPD patterns from (7×7) Si (111), as well as models proposed for the (3×3) and ($\sqrt{3}\times\sqrt{3}$)R30° 6H-SiC reconstructions. Forward scattering features similar to those observed from (7×7) Si (111) were also observed from ($\sqrt{3}\times\sqrt{3}$)R30° 6H-SiC $(0001)_{Si}$ surfaces. However, additional features not observed in (7×7) Si (111) were observed in the ($\sqrt{3}\times\sqrt{3}$)R30° 6H-SiC XPD patterns which were attributed to the substitution of carbon atoms for silicon atoms on the diamond FCC lattice. Unlike (1×1) and (7×7) Si (111) surfaces, differences were observed between the XPD patterns of (3×3) and ($\sqrt{3}\times\sqrt{3}$)R30° SiC $(0001)_{Si}$ surfaces. The most significant difference observed between the (3×3) and ($\sqrt{3}\times\sqrt{3}$)R30° reconstructions was the equivalence of the [10-10] and [01-10] azimuths in the (3×3) structure. The differences between the (3×3) and ($\sqrt{3}\times\sqrt{3}$)R30° XPD patterns were attributed to the presence of an incomplete bilayer of Si the (3×3) surface. The (3×3) SiC XPD patterns observed in this study are consistent with a faulted Si bilayer stacking sequence recently proposed based on STM observations.

I. Introduction

X-ray photoelectron diffraction (XPD) is an exciting new technique for probing the local atomic structure of metal and semiconductor surfaces with atomic specificity [1-3]. XPD experiments essentially consist of performing angle dependent x-ray photoelectron spectroscopy (XPS) measurements. Anisotropies in the angular dependence of the intensity of emitted photoelectrons in XPS are created by interference between other emitted photoelectron waves and/or scattering by nearest neighbor atoms. For the high kinetic energies (≈ 1 keV) typically employed, XPD spectra are dominated by forward scattering (or focusing) of the emitted photoelectron by the potential of the atomic nucleus of nearest neighbor atoms. This effect which can be viewed as a zeroth order approximation to XPD creates intensity enhancements along crystallographic and surface-adsorbate bond directions (see Fig. 1).

Submitted to *Surface Science*

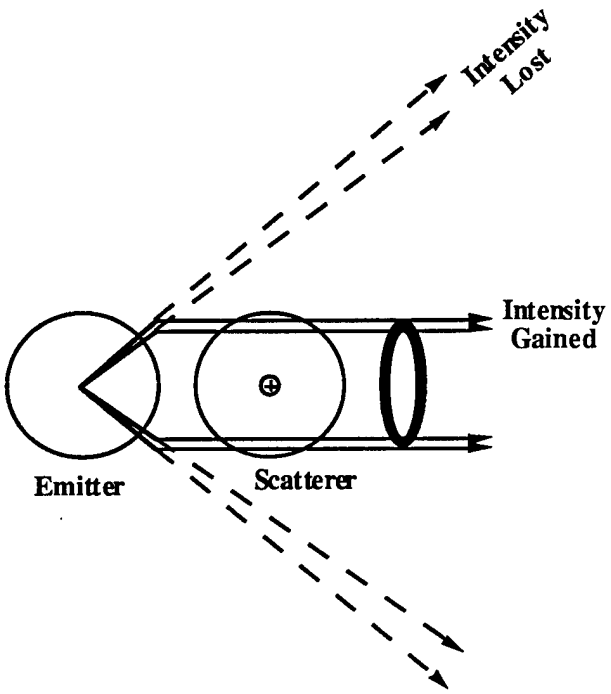

Figure 1. Schematic illustrating forward focusing/scattering effects in x-ray photoelectron diffraction experiments.

Accordingly, this technique has been successfully employed in the determination of surface adsorption sites for various atoms and molecules on metals and semiconductors as well as for studying a number of different epitaxial growth systems [1-6]. Most recently, further developments and enhancements of this technique have actually resulted in the demonstration of holographic images of various metal [7-10] and semiconductor surfaces [11]. In this paper, we apply XPD to study the atomic structure of (3×3) and ($\sqrt{3}\times\sqrt{3}$)R30° reconstructed $(0001)_{Si}$ 6H-SiC surfaces.

Silicon carbide is a wide band gap compound semiconductor (E_g (6H-SiC) = 3.0 eV) which is of considerable importance to the development of high-temperature, high-frequency, and high-power electronic devices [12]. The ability to develop SiC into the material of choice for these applications, however, has been currently limited by the inability to control the types and densities of a variety of line, planar, and macroscopic defects in SiC wafers and films [12]. By analogy to a more thoroughly investigated material such as silicon [13-16], it is conceivable that many of these defects originate and/or nucleate at defects on the SiC surface. Therefore, in order to understand how these defects originate, a detailed understanding of the atomic structure of the SiC surface is needed. For the (0001) surface of 6H-SiC, this has in part been provided by many recent scanning tunneling microscopy (STM) studies [17-24] which have identified a variety of different surface reconstructions ranging from (3×3), ($\sqrt{3}\times\sqrt{3}$)R30°, (9×9), (6×6), and ($6\sqrt{3}\times6\sqrt{3}$)R30°.

By analogy to the group III adatom ($\sqrt{3}\times\sqrt{3}$)R30° Si (111) reconstructed surfaces [25-28], many have proposed that ($\sqrt{3}\times\sqrt{3}$)R30° 6H-SiC (0001) surface reconstructions are due to bulk terminated (0001) 6H-SiC surfaces with a 1/3 ML (monolayer) coverage of silicon or carbon adatoms in the T_4 position (see Fig. 2) [29,30]. Recent STM investigations by Owman and Martensson [19] and Li and Tsong [21] have been able to confirm the three-fold symmetric unit cell, but unfortunately were unable to resolve the chemical identity of the adatom or determine the exact position of the adatom (i.e. T_4 or H_3). However, Owman and Martensson [19] were able to determine that the reconstruction was not composed of a mixture of Si and C adatoms or a mixture of T_4 and H_3 sites (i.e. single adatom on a single site). These findings by

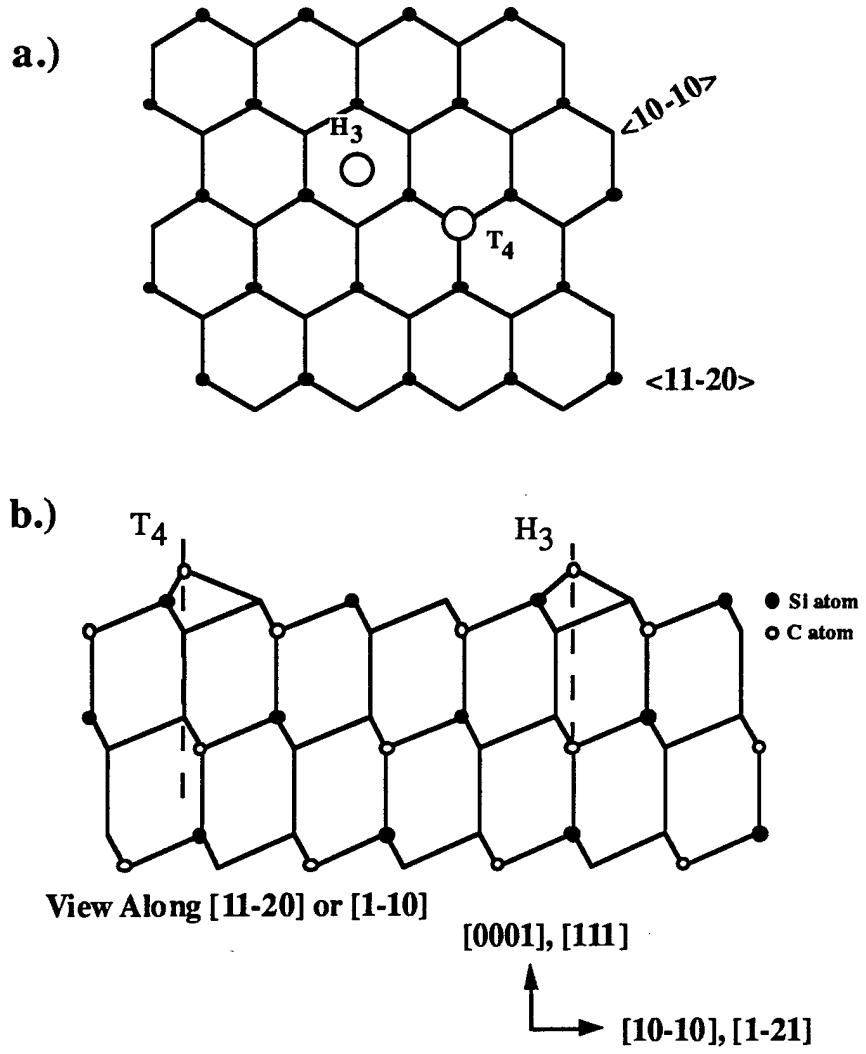

Figure 2. Schematics illustrating various adatom adsorption sites for ($\sqrt{3}\times\sqrt{3}$)R30° reconstructions on (111)/(0001) surfaces. (a) Top down view along [000-1], (b) Side view along [11-20].

Owman and Martensson [19] are complementary to the theoretical results of Northrup and Neugebauer [31]. Their recent supercell calculations using the density functional method have shown that for $(\sqrt{3}\times\sqrt{3})R30°$ (111) 3C-SiC surfaces, Si adatoms are preferred over C adatoms and that the T_4 site is favored over the H_3 site by both Si and C adatoms. These results are consistent with previous calculations by Northrup which showed the T_4 site to be preferred in Si (111) $(\sqrt{3}\times\sqrt{3})R30°$:Si adatom geometries [32].

In contrast, semi-empirical, self consistent quantum mechanical cluster calculations by Badziag [33,34] show that for the $(0001)_{Si}$ $(\sqrt{3}\times\sqrt{3})R30°$ reconstructed surface a hydrogenated triangle of C atoms (i.e. similar to cyclopropane) centered on the T_4 position is energetically more favorable than C or Si adatoms hydrogenated or unhydrogenated. This hydrogenated C_3 model is similar in nature to the milk stool model deduced for $(\sqrt{3}\times\sqrt{3})R30°$ Si (111):Sb surfaces where the Sb atoms form trimers centered on the T_4 site [35,36]. The validity of this model is somewhat questionable since it would require hydrogen to not desorb from the SiC surface until temperatures of > 1150°C at which point the $(\sqrt{3}\times\sqrt{3})R30°$ reconstruction disappears. In defense of his model, Badziag points out that for diamond, hydrogen desorbs at temperatures of 1000 and 1150°C for the (111) [37] and (100) [38] surfaces which is consistent with the observed stability of this reconstruction. However, Allendorf and Outka [39] observed two hydrogen desorption peaks from polycrystalline SiC surfaces at ≈ 700 and 850°C which is well below the temperature at which this reconstruction is observed to occur.

For the (3×3) $(0001)_{Si}$ 6H-SiC surface, Kaplan [29] originally proposed a model based on AES data for a SiC surface terminated by a bilayer of silicon. Based on analogy to the (7×7) Si (111) DAS model, Kaplan proposed a (3×3) unit cell which consisted of two adatoms, six rest atoms (three dimers), and eight silicon atoms in the second layer positioned approximately directly over the silicon atoms of the SiC substrate. However, the recent STM results of Kulakov *et al.* [22] detected only one maxima (i.e. one adatom) in the (3×3) unit cell which is in contrast to the model proposed by Kaplan which would predict two maxima. Based on this discrepancy, Kulakov *et al.* [22] proposed a modified structure which was consistent with the AES results of Kaplan and their STM data. The model for the (3×3) surface proposed by Kulakov *et al.* [22] consists of a unit cell with 1 adatom, 3 rest atoms, and 7 silicon atoms located approximately on top of the silicon atoms of the SiC surface (see Fig. 3). This model includes 3 dimers and three dangling bonds (two unsatisfied Si bonds from the SiC substrate, and 1 dangling bond from the adatom) compared to the 4 dangling bonds in the model by Kaplan [29]. However, Kulakov *et al.* [22] did observe stacking faults in their (3×3) reconstructed surface which had a structure essentially like that of the (3×3) model proposed by Kaplan [29] (see Fig. 4). Using STM, Li and Tsong [21] also confirmed the presence of one maxima in the (3×3) unit cell but, in contrast, concluded that the (3×3) reconstruction consisted

of only 4/9 ML coverage of silicon for the $(0001)_{Si}$ 6H-SiC surface. Accordingly, they attributed the (3×3) surface to extra Si-C tetrahedra on the surface distributed in a 3×3 pattern (see Fig. 5) rather than a bilayer of silicon.

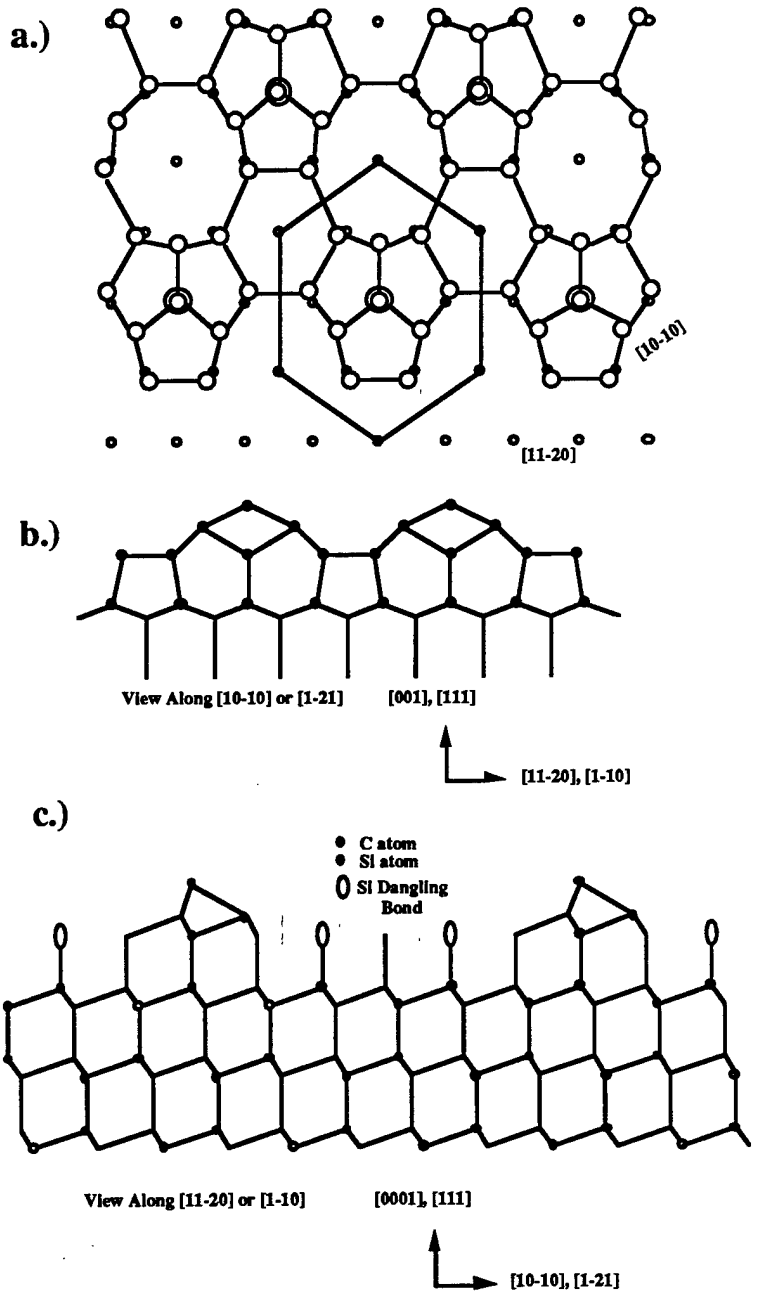

Figure 3. Model proposed by Kulalov *et al.* [22] for the (3x3) reconstructed $(0001)_{Si}$ 6H-SiC surface. (a) Top down view along [000-1], (b) side view along [11-20], and (c) [10-10].

In this paper, we report the first XPD patterns obtained from $(0001)_{Si}$ 6H-SiC surfaces. The XPD patterns obtained from the (3×3) and $(\sqrt{3}\times\sqrt{3})R30°$ $(0001)_{Si}$ 6H-SiC surfaces are compared with those obtained from (7×7) (111) Si surfaces and the proposed models for these SiC reconstructions. Based on this data, we are able to support only some of the proposed models for these reconstructions. Estimates of the experimental inaccuracies possible in XPS experiments due to anisotropies in the angular dependence of the intensity of Si 2p and C 1s photoemission are also provided by this data.

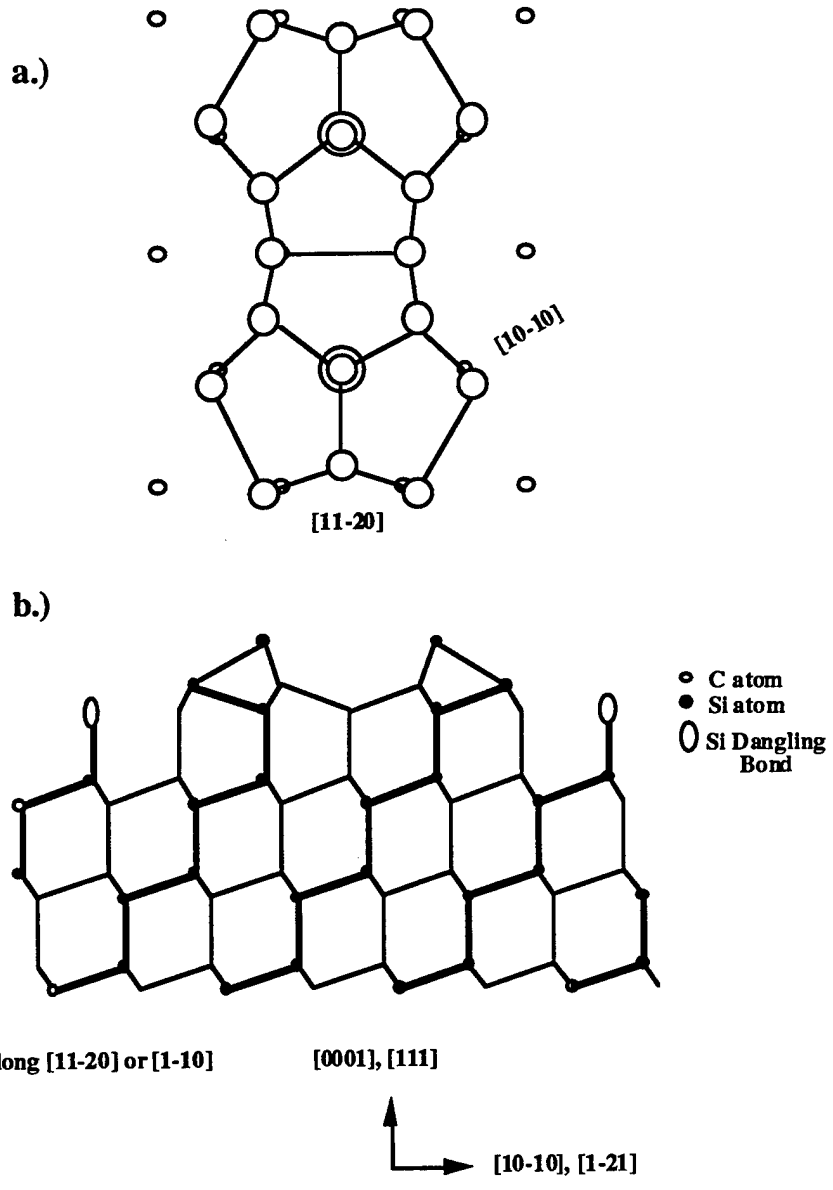

Figure 4. Model proposed by Kaplan [29] for the (3×3) reconstructed $(0001)_{Si}$ 6H-SiC surface. (a) Top down view along [000-1], (b) side view along [11-20].

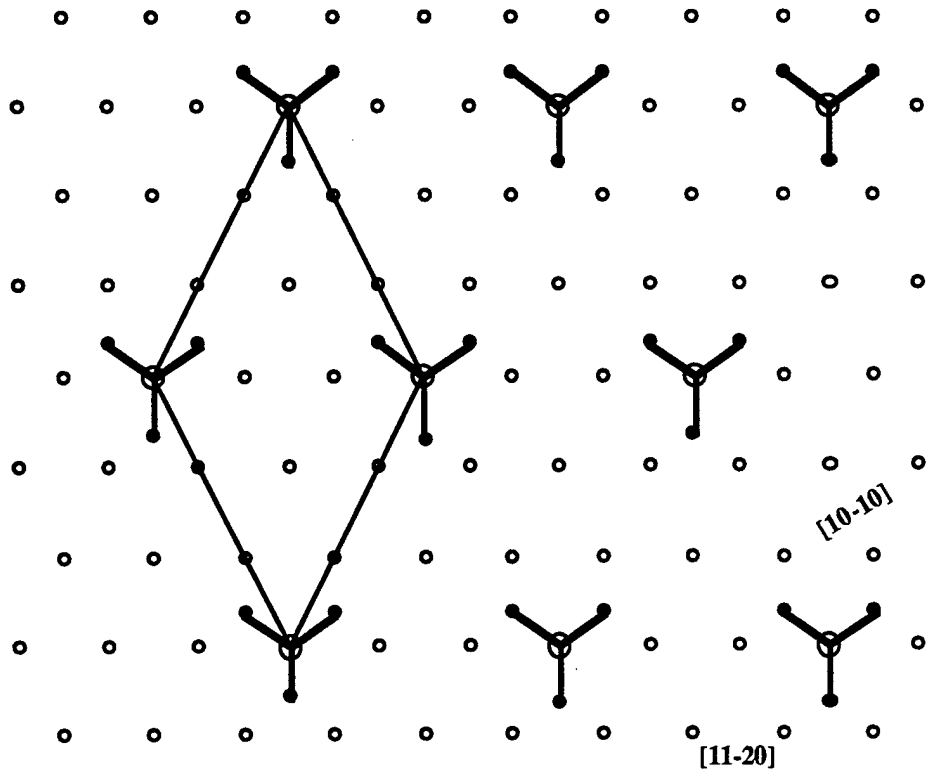

Figure 5. Top down view of model proposed by Li and Tsong [21] for the (3×3) reconstructed $(0001)_{Si}$ 6H-SiC surface.

II. Experimental Procedure

The experiments described in this paper were conducted in an integrated surface analysis and growth system which has been previously described [40,41]. In this study, only the XPS and SiC ALE systems were used. The n-type ($N_d=10^{18}/cm^3$), off axis (4° toward {11-20}) $(0001)_{Si}$ 6H-SiC wafers used in this research were supplied by Cree Research, Inc. with an ≈ 1 μm n-type 6H epilayer ($N_d=10^{17}/cm^3$) and a 1000Å thermally grown oxide. The back side of the SiC wafer was sputter coated with tungsten after removal of the thermal oxide with a 10 min. dip in 10:1 HF. The back side tungsten coating was necessary in order to improve the heating efficiency of the SiC wafer by our tungsten filament heater as SiC is transparent in the infra-red. Prior to insertion into the SiC ALE system, the SiC wafers were given an *ex situ* clean consisting of ultrasonification in trichloroethylene, acetone, and methanol for 10 min. each, followed by a 10 min. 10:1 buffered HF vapor clean to remove any native oxides. The SiC wafer was then loaded into the SiC ALE system and annealed in 10^{-6} Torr SiH_4 for 15 min. at 1050°C. This produced an oxygen free (3×3) reconstructed surface. The $(\sqrt{3}\times\sqrt{3})R30°$ reconstruction was generated by annealing the (3×3) surface in UHV in the ALE

system at 1050°C for ≈ 10 min. Additional details regarding our sample preparation and procedure have been previously published [40-42,43].

After either the (3×3) or ($\sqrt{3}\times\sqrt{3}$)R30° surface had been prepared, the SiC wafer was transferred *in situ* to the XPS system. XPD patterns were acquired in this system by rotating the SiC wafer about various polar and azimuthal angles using a computer driven goniometer with five degrees of freedom (x,y,z,θ, and ϕ) while the positions of the x-ray source and electron energy analyzer were fixed. Though the angular acceptance of the lens of the electron energy analyzer (VG CLAMII) was ± 7°, an angular resolution of ≈ ±1° was achieved by geometric constraints via grounding the lens and using smaller channeltron acceptance slits. The SiC XPD patterns were acquired by monitoring the Si 2p and C 1s core levels photoexcited by Al Kα radiation ($h\nu$ = 1486.6 eV). The kinetic energy of these photoelectrons (≈ 1380 and 1203 eV respectively) was sufficiently high that forward scattering effects should be dominant and probe ≈ 20Å of the SiC surface. Polar scans along high symmetry azimuths were acquired in increments of 0.9° from -35° to 70°. The wafer flat provided by Cree was used to locate the various azimuths and is of the {10-10} family of planes. The data presented is the raw angular distribution of the measured intensity of the Si 2p and C 1s core levels. No attempts were made to correct for background, variation in sampling depth, or surface area seen by the electron energy analyzer. To ensure that the system was operating properly, XPD spectra were first acquired from Si (100) and Si (111) surfaces and compared with previously published high resolution XPS spectra for these surfaces [44-48]. Figure 6 displays an XPD spectrum from a (2×1) Si (001) surface along the [110] azimuth. As illustrated, sharp features with FWHM ≅ 3° were easily resolved and were found to be in excellent agreement with previously reported results for this surface [48].

III. Results

Figures 7-11 show various Si 2p and C 1s XPD patterns obtained from (7×7) Si (111), and (3×3) and ($\sqrt{3}\times\sqrt{3}$)R30° 6H-SiC $(0001)_{Si}$ surfaces. These patterns were acquired along high symmetry azimuths such as [10-10], [11-20], and [01-10] azimuths (note $\langle 1\text{-}21\rangle_{cub} = \langle 10\text{-}10\rangle_{hex}$ and $\langle 1\text{-}10\rangle_{cub} = \langle 11\text{-}20\rangle_{hex}$). As shown in these figures, peaks of varying FWHM were observed. Generally speaking, diffraction structures of FWHM ≈ 10-20° are consistent with forward scattering features associated with crystallographic directions or nearest neighbor atoms [1-3]. Narrow peaks or wide peaks with fine structure of ≈ 3° are usually due to scattering from more distant atoms or complex/higher order interference phenomena [1-3].

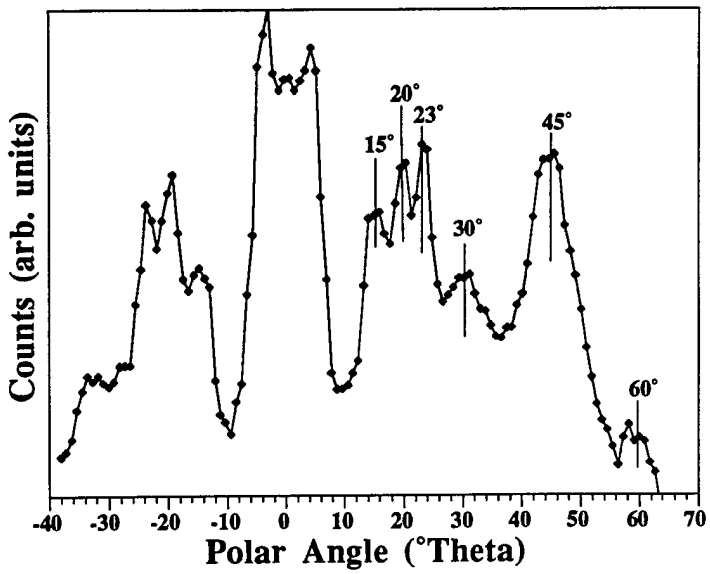

Figure 6. XPD pattern from (2×1) Si (100) along the [110] azimuth.

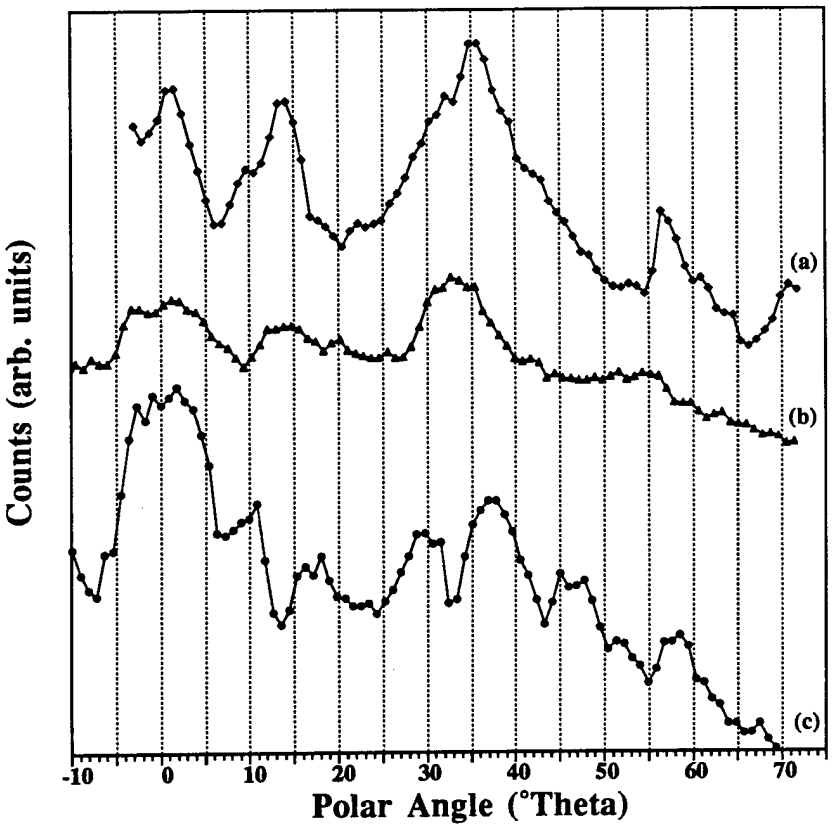

Figure 7. Si 2p x-ray photoelectron diffraction pattern along [1-21]/[10-10] azimuths from (a) (7×7) Si (111), (b) (3×3) 6H-SiC $(0001)_{Si}$, and (c) $(\sqrt{3}\times\sqrt{3})R30°$ $(0001)_{Si}$ 6H-SiC.

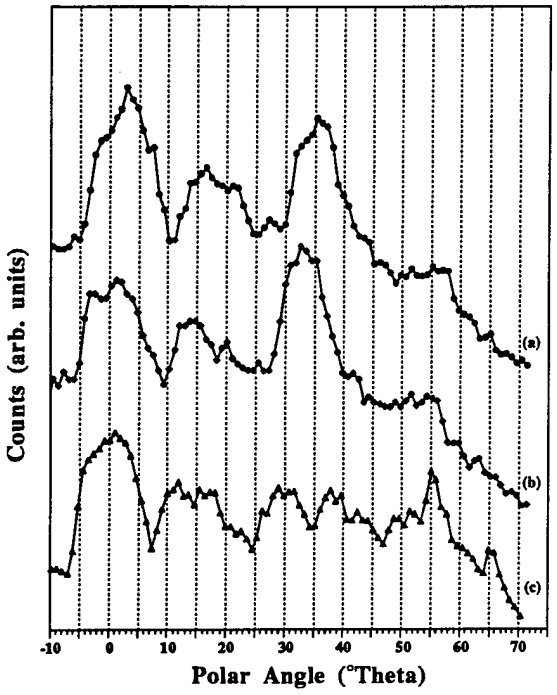

Figure 8. Si 2p x-ray photoelectron diffraction patterns from (a) (3×3) 6H-SiC $(0001)_{Si}$ along [01-10], (b) (3×3) 6H-SiC $(0001)_{Si}$ along [10-10], and (c) $(\sqrt{3}\times\sqrt{3})R30°$ 6H-SiC $(0001)_{Si}$ along [01-10].

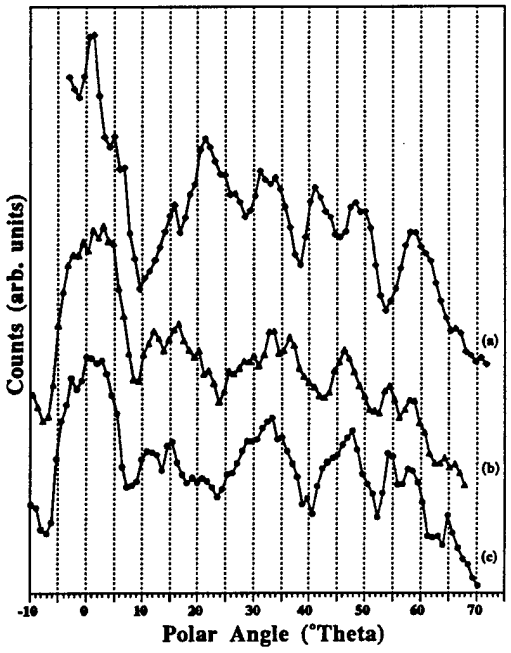

Figure 9. Si 2p x-ray photoelectron diffraction patterns along [-110]/[11-20] from (a) (7×7) Si (111), (b) (3×3) 6H-SiC $(0001)_{Si}$, and (c) $(\sqrt{3}\times\sqrt{3})R30°$ 6H-SiC $(0001)_{Si}$.

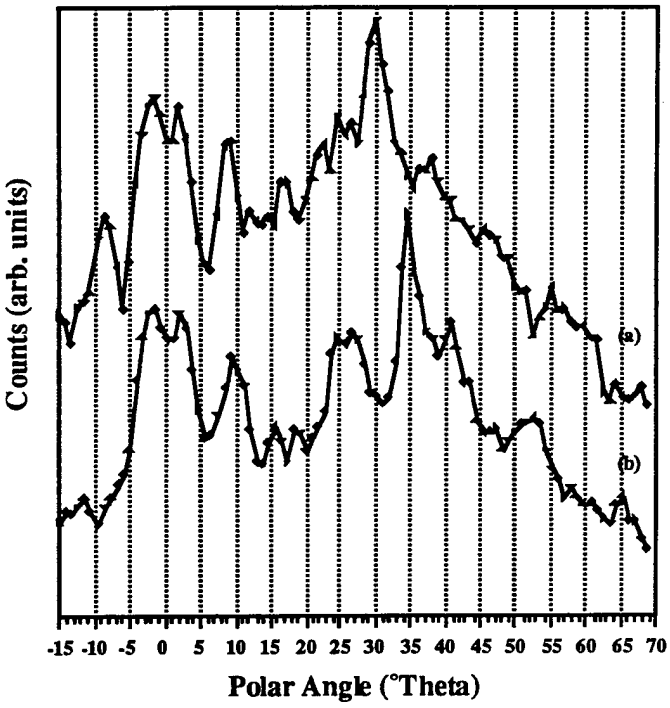

Figure 10. C 1s XPD patterns from $(\sqrt{3}\times\sqrt{3})R30°$ 6H-SiC $(0001)_{Si}$ along (a) [01-10], and (b) [11-20].

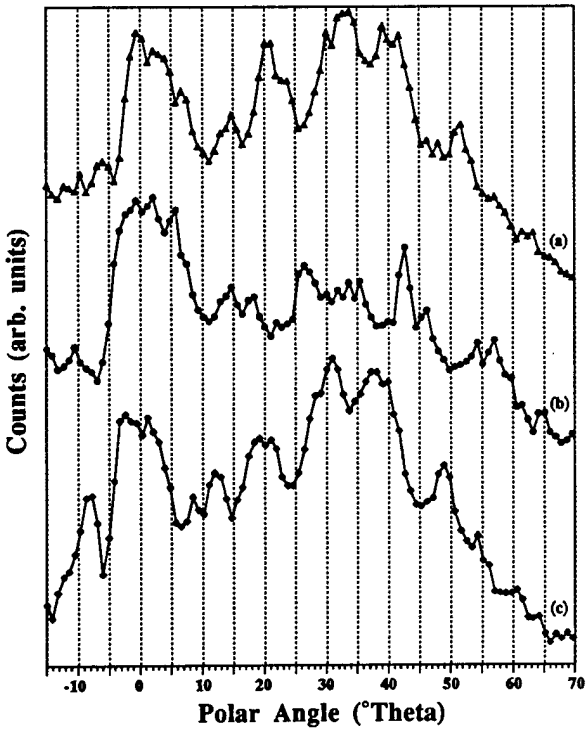

Figure 11. C 1s XPD patterns from (3×3) 6H-SiC $(0001)_{Si}$ along (a) [10-10], (b) [11-20], and (c) [10-10] azimuths.

In order to determine which peaks in the XPD spectra were due to forward scattering effects, we next consider the atomic structure of the $(0001)_{Si}$ 6H-SiC surface. SiC is a unique material that exhibits several different polymorphs which differ only in the stacking sequence along the c axis. This particular phenomena is referred to as polytypism, and as many as 256 different polytypes of SiC have been reported. However, only a few polytypes, 3C, 4H, 6H, and 15R are commonly observed. In the Ramsdell notation used to describe these polytypes, the preceding number represents the number of Si-C bilayers needed to repeat the stacking sequence along [111]/[0001] directions and the following letter describes the crystal structure (i.e. C = cubic, H = hexagonal, and R = rhombohedral). In the case of 6H-SiC, the H is deceiving as 6H-SiC is actually 66.6% cubic and exhibits an ABCB'C'A' stacking sequence which is similar to that of 3C-SiC differing only in the periodic stacking fault in the 6H structure (see Fig. 12). Accordingly, in a surface sensitive technique such as XPD which effectively only samples the first 10Å of the surface, (0001) 6H and (111) 3C-SiC should be essentially indistinguishable. Therefore, for simplicity sake, we will treat the (0001) 6H XPD spectra as if it were from (111) 3C-SiC. This is fortuitous as 3C-SiC and Si and have similar crystal structures and therefore comparisons can be made between XPD spectra from (111) Si and (111)/(0001) 3C/6H-SiC. Based on these considerations, the expected peaks for forward scattering/focusing along certain crystallographic directions for bulk terminated (111) 3C-SiC, and $(0001)_{Si}$ 6H-SiC surfaces are listed in Table I (see Figs. 13 and 14). Table I presents the forward scattering peaks expected from both C 1s and Si 2p photoelectrons. In the case of Si (111), the C 1s forward scattering peaks would be expected to appear in Si 2p XPD patterns as the carbon atoms have been replaced by Si atoms.

Table I. Expected Forward Scattering/Focusing Peaks from Bulk Terminated (111) Si, (111) 3C-SiC, and $(0001)_{Si}$ 6H-SiC Surfaces Along [10-10], [11-20], and [01-10] Azimuths.

Si 2p			
[10-10]	[11-20]	[01-10]	Scatterer
35.3°			Si
		54.7°	Si
	58.5°		C
70.5°			C-Si
	72.9°		C

C 1s			
[10-10]	[11-20]	[01-10]	Scatterer
		29.5°	Si
	31.4°		Si
35.3°			C
	44.4°		Si
		54.7°	C
70.5°			Si

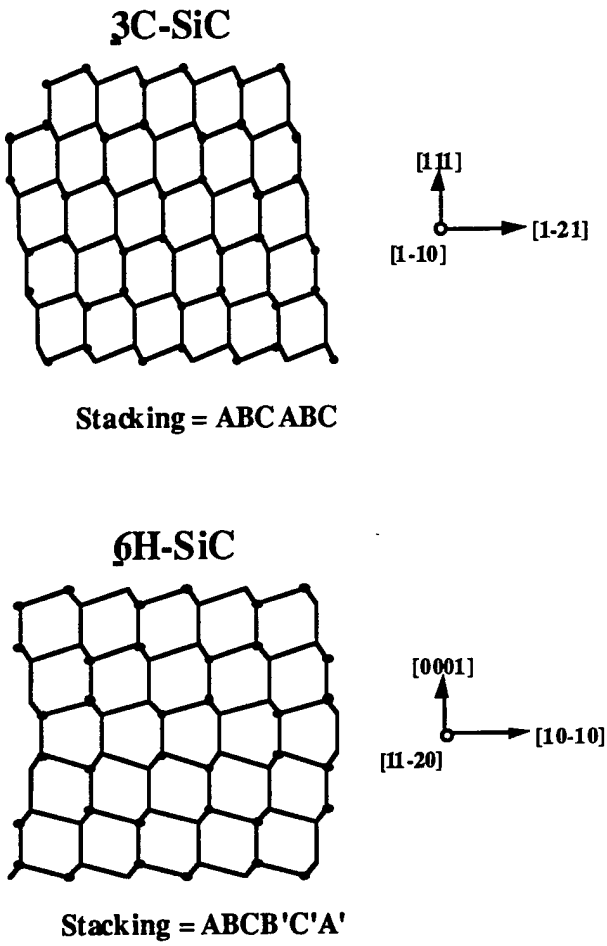

Figure 12. Schematic illustrating the differences in stacking along the [111]/[0001] direction for 3C and 6H-SiC.

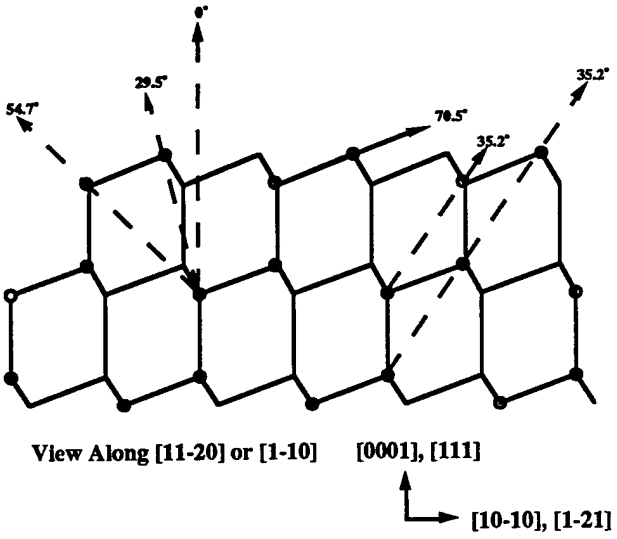

Figure 13. Schematic illustrating expected forward scattering/focusing peaks in XPD along the [11-20] azimuth of 3C/6H-SiC.

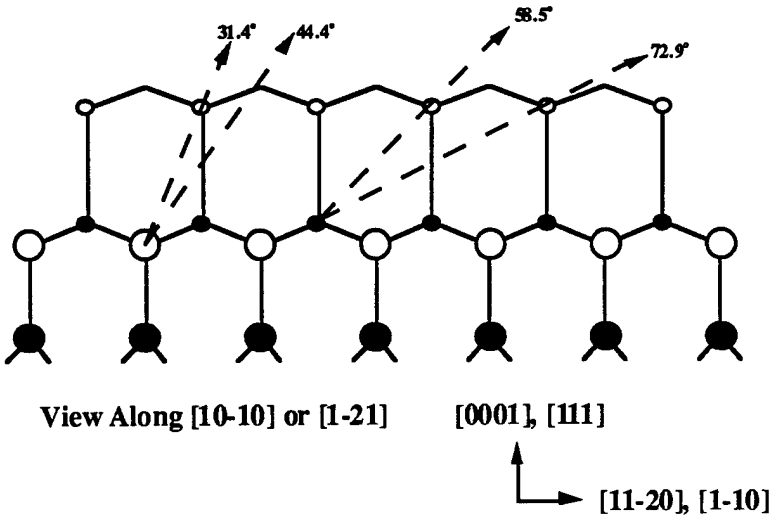

Figure 14. Schematic illustrating expected forward scattering/focusing peaks in XPD along the [10-10] azimuth for 3C/6H-SiC.

$(\sqrt{3}\times\sqrt{3})R30°$ $(0001)_{Si}$ 6H-SiC. For Si 2p XPD patterns obtained from $(\sqrt{3}\times\sqrt{3})R30°$ 6H-SiC $(0001)_{Si}$ surfaces, most of the expected forward scattering peaks were identified. In the [10-10] azimuth (see Fig. 7c), a broad/intense peak at 36-37° was identified as expected. This peak was similar to and consistent with forward scattering along the [011]/[10-11] crystallographic axes (i.e. the Si-C atomic row). However, unlike the (7×7) Si (111) surface, broad/intense peaks at 19 and 42° were symmetrically observed on both sides of the [011]/[10-11] forward scattering peak. As mirror symmetry is expected about the [011] atomic row due to (100) glide planes [44], these additional peaks are probably due to higher order interference phenomena or forward scattering from larger emitter-scatterer distances. Similar to (7x7) Si (111), peaks of this nature were also observed at 15 and 59° in Si 2p XPD patterns along the [10-10] azimuth. However, in contrast to (7×7) Si (111), a forward scattering peak at 70.5° was not observed. In the case of Si (111), this peak is due to forward scattering along the (11-1) crystallographic direction. The absence of this peak from $(\sqrt{3}\times\sqrt{3})R30°$ 6H-SiC $(0001)_{Si}$ surfaces may be related to the fact that (0001) and (000-1) are not equivalent directions in SiC but are equivalent directions in Si.

C 1s XPD patterns obtained along the [10-10] azimuth showed a single sharp peak at 30° which is 5° off from the expected value of 35° for forward scattering along the [011]/[10-11] atomic row (see Fig. 10a). This discrepancy, however, may be related to the fact that the 35° peak would be expected based on forward scattering by carbon atoms. Carbon has a smaller atomic nucleus and should be expected to be a weaker scatterer. Therefore, the position of this forward scattering peak maybe determined more by silicon atoms along the [011]/[10-11] row.

Like Si (111), asymmetry's were observed between Si 2p XPD spectra acquired along <10-10> and <01-10> azimuths of ($\sqrt{3}\times\sqrt{3}$)R30° 6H-SiC $(0001)_{Si}$ (i.e. <10-10> ≠ <01-10>). In the [01-10] azimuth, the expected peak for forward scattering in the [100] direction was observed at 55°C (see Figure 8c). Similar to Si 2p XPD patterns along [-12-1] azimuths [44], peaks due to complex/higher order interference phenomena were also observed from 10-40° in the [01-10] azimuth of ($\sqrt{3}\times\sqrt{3}$)R30° 6H-SiC $(0001)_{Si}$ surfaces. However, unlike Si, symmetry was not observed about this peak.

In the [11-20] azimuth, a mosaic of broad diffraction peaks of equal intensity were observed from Si 2p XPD patterns from the ($\sqrt{3}\times\sqrt{3}$)R30° 6H-SiC $(0001)_{Si}$ surface (see Fig. 9c). Most of the peaks observed in the Si 2p XPD pattern from (7×7) Si (111) observed along the [1-10] azimuth were also observed in the Si 2p XPD patterns along the [11-20] azimuth from the ($\sqrt{3}\times\sqrt{3}$)R30° 6H-SiC $(0001)_{Si}$ surface. However, the peak at 58.5° expected for forward scattering along the [-131] direction was observed to have a volcano shape for ($\sqrt{3}\times\sqrt{3}$)R30° 6H-SiC $(0001)_{Si}$ surface and a rounded shape for the (7×7) Si (111) surface. In fact, rounded peaks from the Si (111) surface along [-110] were observed to have a volcano shape in the [11-20] azimuth of the SiC surface (and vice versa). The C 1s XPD patterns obtained along the [11-20] azimuth showed strong peaks at 25, 35, and 52.5° (see Fig. 10b). The sharpest/most intense peak at 35° is slightly off from the expected value of 31.4° for scattering by a top layer carbon atom (see Fig. 14). However, this can be expected as the scattering carbon atom does not actually lie in the (10-10) plane.

The maximum anisotropy in intensity observed in both the Si 2p and C 1s XPD patterns was observed about the 0°/[0001] forward scattering peak. For Si 2p and C 1s the maximum anisotropy $(I_{max}-I_{min})/I_{max}$ was ≈ 65 and 40 % respectively. Similar to (7×7) Si (111), higher order diffraction effects were also observed at 10-15° on both sides of the Si 2p and C 1s 0°/[0001] forward scattering peaks. However, in contrast to Si (111), the Si 2p 0°/[0001] forward scattering peak from $(0001)_{Si}$ 6H-SiC surfaces does not exhibit a volcano type shape but rather a flat sawtooth type shape (see Fig. 8a). The C 1s 0°/[0001] forward scattering peak from $(0001)_{Si}$ 6H-SiC does exhibit a volcano shape (see Fig. 10a). A similar effect has been observed between Si 2p and C 1s spectra from (001) Si and 3C-SiC [48-50]. The shape of this peak is strongly affected by the presence of scattering atoms surrounding the [111]/[0001] direction. As silicon is the nearest neighbor atom to carbon along the [0001] direction, scattering by these silicon atoms probably induces the volcano shape observed in the C 1s XPD. For silicon atoms in SiC, carbon is the nearest neighbor atom, but the scattering factor of carbon is much weaker, hence the sawtooth structure. However, in pure silicon and diamond, all the atoms are either silicon or carbon and the volcano shape reappears [44-48,51]. The also explains many of the differences between Si 2p XPD spectra from Si and SiC along the [11-20] azimuth. Finally, it should be mentioned that the centroid of the Si 2p and

C 1s 0°/[0001] forward scattering peaks were observed to vary by ± 2°. As this variation was not observed from on axis (001) and (111) Si substrates, the variation in the position of [0001] in the polar scans is probably related to the fact that the SiC wafers were 4° off axis in the <11-20> direction and not related to drift in our sample stage.

(3×3) $(0001)_{Si}$ 6H-SiC. In contrast to reconstructed and unreconstructed diamond and silicon surfaces [44-48,51], significant differences were observed between the Si 2p XPD patterns from (3×3) and (√3×√3)R30° 6H-SiC $(0001)_{Si}$ surfaces. For instance, the [011]/[101-1] forward scattering peak at ≈ 33° was observed from [10-10] Si 2p XPD patterns from both (3×3) and (√3×√3)R30° 6H-SiC surfaces (see Fig. 7b, c). However, peaks centered symmetrically at 29 and 46° about the [011]/[101-1] forward scattering feature were not observed from the (3×3) surface (see Fig. 7b) which is more similar to Si 2p XPD patterns from Si (111) in this azimuth (see Fig. 7a). Additionally, the sharp higher order diffraction peaks at 9-18 and 58° observed from the (√3×√3)R30° surface were observed to be more broad and less intense for the (3x3) surface. Similar differences were also seen in the (3×3) C 1s XPD patterns in the [10-10] azimuth. In this case, a volcano shaped peak centered at 35° was observed in [10-10] C 1s XPD patterns from the (3×3) surface instead of the one sharp peak centered at 30° observed from the (√3×√3)R30° 6H-SiC surface (see Fig. 11c). Sharper peaks centered symmetrically about the 35° volcano peak at 20 and 59° were also observed in the (3×3) [10-10] C 1s XPD patterns.

In the [11-20] azimuth, a mosaic of sharp higher order diffraction features were observed in C 1s XPD patterns from the (3×3) surface instead of the single sharp peak centered at 35° observed in the (√3×√3)R30° XPD patterns (see Fig. 11b). However for [11-20] Si 2p XPD patterns, there were not any significant differences between the (3×3) and (√3×√3)R30° 6H-SiC surfaces (see Fig. 9b,c). Finally in Si 2p XPD patterns, the 0°/[0001] forward scattering peak was observed to be volcano shaped for the (3x3) surface whereas this peak exhibited a sawtooth/rounded shape for the (√3×√3)R30° 6H-SiC surface (see Figs. 7(b),(c) and 8(b),(c)). The opposite, however, was observed in C 1s XPD patterns where a volcano shaped 0°/[0001] forward scattering peak was observed from the (√3×√3)R30° surface whereas a sawtooth/rounded peak was observed from the (3×3) surface (see Figs. 10 and 11).

Perhaps the largest differences between XPD of (3×3) and (√3×√3)R30° 6H-SiC surfaces are found in the [01-10] azimuth. As can be seen in Figs. 8(a),(b) and 11(a),(c), Si 2p and C 1s XPD patterns from the (3×3) 6H-SiC surface along the [01-10] and [10-10] azimuths are identical. This is in complete contrast, to the (√3×√3)R30° 6H-SiC surface in which the [10-10] and [01-10] azimuths were observed to be completely different (i.e. asymmetric about [0001] along <10-10>). The equivalence of the [10-10] and [01-10] directions for the (3×3) 6H-SiC surface suggests drastic changes in the surface structure of the SiC which will be discussed further in the next section.

IV. Discussion

$(\sqrt{3}\times\sqrt{3})R30°$ $(0001)_{Si}$ 6H-SiC. As some peaks were observed in XPD patterns from $(\sqrt{3}\times\sqrt{3})R30°$ $(0001)_{Si}$ 6H-SiC which had not been previously observed from Si (111) surfaces, attempts were initially made to see if these extra peaks could be assigned to forward scattering/diffraction due to silicon or carbon adatoms on the surface. As previously mentioned, adatoms in T_4 or H_3 sites are commonly believed to be the origin of the $(\sqrt{3}\times\sqrt{3})R30°$ reconstruction. Table II lists the additional expected forward scattering peaks due to Si or C adatoms based on various different models proposed for the $(\sqrt{3}\times\sqrt{3})R30°$ reconstruction [31-34]. Unfortunately, we were not able to determine with any certainty whether any of these peaks truly existed. Therefore, single scattering cluster simulations are probably necessary in order to determine the exact structure of the $(\sqrt{3}\times\sqrt{3})R30°$ reconstruction based on XPD data. However, the authors note that Pirri *et al.* [44] and Kuttel *et al.* [51] have experienced similar difficulties in distinguishing between XPD patterns from (7×7) and (1×1) Si (111) and (2×1) and (1×1) Diamond (111), respectively.

Table II. Expected Si 2p and C 1s Photoelectron Diffraction Peaks for Adatom Scattering in T_4 and H_3 Positions Based on Data of Northrop and Neugebauer [31] and Badziag [34] for $(\sqrt{3}\times\sqrt{3})R30°$ $(0001)_{Si}$ 6H-SiC.

Si adatom, T_4
Northrop & Neugebauer [31]

<10-10>		<11-20>		<-1010>	
Si 2p	C 1s	Si 2p	C 1s	Si 2p	C1s
	66.9°	56.0		45.2°	
65.2°			53.6°		
52.1°		43.2°			
	20.1°		36.5°		

C adatom, T_4
Northrop & Neugebauer [31]

<10-10>		<11-20>		<-1010>	
Si 2p	C 1s	Si 2p	C 1s	Si 2p	C1s
71.8°		59.1°		53.8°	
55.3°			56.1°		
22.3°	40.6°				

C_3 Model
Badziag [34]

<10-10>		<11-20>	
Si 2p	C 1s	Si 2p	C 1s
68.8°			48°
33.3°		37.9°	
	27.3°		20.2°
	17.0°	14.5°	
9.5°			

(3×3) $(0001)_{Si}$ 6H-SiC. As mentioned above, significant differences were observed between Si 2p and C 1s XPD patterns from the (3×3) and ($\sqrt{3}\times\sqrt{3}$)R30° 6H-SiC $(0001)_{Si}$ surfaces. Perhaps, the most striking difference was the observed equality of the [10-10] and [01-10] azimuths for the (3×3) reconstruction and the inequality of these azimuths for the ($\sqrt{3}\times\sqrt{3}$)R30° reconstruction. In order to gain further insight into the nature of these differences, comparisons were made to previously proposed models for the (3×3) reconstruction based on recent STM images [21,22]. Based on these models, a new set of forward scattering peaks were calculated/estimated for the (3×3) reconstruction and which are presented in Table III. As discussed in the introduction, Li and Tsong [21] have proposed that the (3×3) reconstruction is a result of 4/9 ML absorption of Si-C tetrahedra arranged in a (3×3) pattern (see Fig. 5). As can be seen in Fig. 5 and Table III, this model does not predict equivalence of the [10-10] and [01-10] azimuths. This model is also in disagreement with our previous observation of a Si-Si Si 2p bonding peak in XPS which indicated a partial bilayer of silicon on the (3×3) SiC surface [40].

Based on the previous AES data of Kaplan [29] and their STM data, Kulakov *et al.* [22] proposed a different model for the (3×3) reconstruction which consisted of an incomplete bilayer of Si. We find this model for the (3×3) reconstruction to be in better agreement with our observed XPS and XPD patterns. First, this is clearly consistent with our observation of a Si-Si Si 2p bonding peak in XPS. As can be seen in Fig. 3c, this model also specifically adds an additional Si-Si bilayer to the [011]/[10-11] atomic row. As silicon has a larger nucleus it should be a more effective scatterer than carbon. Therefore, the addition of the Si-Si bilayer should enhance the intensity along the [011]/[10-11] chain due to increased forward scattering. This is exactly what we observe in both our C 1s and Si 2p [10-10] XPD patterns. Unfortunately, the model proposed by Kulakov et al fails to explain the observed equality of our [10-10] and [01-10] Si 2p and C 1s patterns. However, we do note that the model originally proposed by Kaplan [29] for the (3×3) reconstruction would explain the equivalence of the [10-10] and [01-10] XPD patterns (see Fig. 4). This is primarily a result of the stacking fault in this structure which produces Si-Si bilayers oriented in both the [10-10] and [01-10] directions. The presence of this structure on SiC surfaces has actually been confirmed by Kulakov *et al.* [22] were they observed faults or domains of different orientation in STM images of the (3×3) surface. The stacking structure in these domains are consistent with the model originally proposed by Kaplan for the (3×3) reconstruction [29]. Unfortunately however, at this stage it is difficult to determine with certainty whether our observations of the equivalence between [10-10] and [01-10] in XPD are due to these stacking faults.

Table III. Estimated Forward Scattering Peaks for (3×3) Reconstructed (111)/(0001) 3C/6H-SiC Surfaces Based on Models Proposed by Kulakov *et al.* [22] and Li and Tsong [21].

Si 2p					
Kulakov			Li & Tsong		
[11-20]	[10-10]	[01-10]	[11-20]	[10-10]	[01-10]
59.3°	66.2°	66.2°	59.3°	66.2°	48.6°
51.5°	53.7°	53.7°	52.6°	29.5°	
42.9°	29.5°	48.6°	42.9°		
38.2°					
33.2°					
C 1s					
Kulakov			Li & Tsong		
[11-20]	[10-10]	[01-10]	[11-20]	[10-10]	[01-10]
59.4°	43.3°	38.0°	58.5°	43.3°	58.5°
39.3°	30.8°	30.8°	39.3°	30.8°	
27.3°	21.3°	25.3°			
25.3°					

V. Conclusion

High resolution (±1°) x-ray photoelectron diffraction (XPD) patterns were obtained along high symmetry azimuths of (3×3) and ($\sqrt{3}\times\sqrt{3}$)R30° reconstructed $(0001)_{Si}$ 6H-SiC surfaces. The data obtained were compared to previously reported XPD patterns from (7×7) Si (111) as well as models proposed models for the (3×3) and ($\sqrt{3}\times\sqrt{3}$)R30° 6H-SiC reconstructions. Forward scattering features similar to those observed from (7×7) Si (111) were also observed from ($\sqrt{3}\times\sqrt{3}$)R30° 6H-SiC $(0001)_{Si}$ surfaces. However, additional features not observed in (7×7) Si (111) were observed in the ($\sqrt{3}\times\sqrt{3}$)R30° 6H-SiC XPD patterns which were attributed to the substitution of carbon atoms for silicon atoms on the diamond FCC lattice. Unlike (1×1) and (7×7) Si (111) surfaces, differences were observed between the XPD patterns of (3×3) and ($\sqrt{3}\times\sqrt{3}$)R30° SiC $(0001)_{Si}$ surfaces. The most significant difference observed between the (3×3) and ($\sqrt{3}\times\sqrt{3}$)R30° reconstructions was the equivalence of the [10-10] and [01-10] azimuths in the (3×3) structure. The faulted (3×3) structure proposed by Kulakov *et al.* [22] was found to be consistent with the (3×3) XPD patterns presented here.

VI. Acknowledgments

The authors would like to thank Cree Research, Inc. for supplying the 6H-SiC wafers. The authors would also like to thank the REU program for partially sponsoring this effort. Meaningful discussions regarding experimental setup with Dr. Egelhoff are also noted. The

research was supported by ONR under contract and the Department of Education via an Electronic Materials/GAANN fellowship.

VII. References

1. W. F. Egelhoff, Jr., Crit. Rev. in Solid State and Materials Sciences **16**, 213 (1990).
2. S. A. Chambers, Surface Science Reports **16**, 261 (1992).
3. S. A. Chambers, Adv. in Physics **40**, 357 (1991).
4. D. A. Wesner, F. P. Coenen, and H. P. Bonzel, Phys. Rev. B **33**, 8837 (1986).
5. M. Seelmann-Eggbert, G. P. Carey, R. Klauser, and H. J. Richter, Surface Science **287/288**, 495 (1993).
6. M. Diani, D. Aubel, J.L. Bischoff, L. Kubler, and D. Bolmont, Surface Science **29**, 110 (1993).
7. G. R. Harp, D. K. Saldin, and B. P. Tonner, Phys. Rev. Lett. 65, 1012 (1990).
8. B. P. Tonner, Z. L. Han, G. R. Harp, and D. K. Saldin, Phys. Rev. B **43**, 14423 (1991).
9. G. R. Harp, D. K. Saldin, and B. P. Tonner, Phys. Rev. B **42**, 9199 (1990).
10. A. Stuck, D. Naumovic, H. A. Aebischer, T. Greber, J. Osterwalder, and L. Schlapbach, Surface Science **264**, 380 (1992).
11. G. S. Herman, S. Thevuthasan, T. T. Tran, Y.J. Kim, and C.S. Fadley, Phys. Rev. Lett. **68**, 650 (1992).
12. R. F. Davis, G. Kelner, M. Shur, J. Palmour, J. A. Edmond, Proc. of the IEEE **79**, 677 (1991).
13. M. K. Sanganeria, M. C. Ozturk, G. Harris, K. E. Violette, I. Ban, C. A. Lee, and D. M. Maher, J. Electrochem. Soc. **142**, 3961 (1995).
14. B. S. Meyerson, E. Ganin, D. A. Smith, and T. N. Nguyen, J. Electrochem. Soc. **133**, 1232 (1986).
15. G. R. Srinivasan and B. S. Meyerson, J. Electrochem. Soc.**134**, 1518 (1987).
16. W. Kern, J. Electrochem. Soc. **137**, 1887 (1990).
17. C. S. Chang, I. S. T. Tsong, Y. C. Wang, and R. F. Davis, Surface Science **256**, 354 (1991).
18. M. A. Kulakov, P. Heuell, V. F. Tsvetkov, and B. Bullemer, Surface Science **315**, 248 (1994).
19. F. Owman, P. Martensson, Surface Science, 330 (1995) L639.
20. Y. Marumoto, T. Tsukamoto, M. Hirai, M. Kusaka, M. Iwami, T. Ozawa, T. Nagamura, and T. Nakata, Jpn. J. Appl. Phys. **34**, 3351 (1995).
21. L. Li, and I.S.T. Tsong, Surface Science **351**, 141 (1996).
22. M. A. Kulakov, G. Henn, B. Bullemer, Surface Science **346**, 49 (1996).
23. S. Tanaka, R. S. Kern, R. F. Davis, J. F. Wendelken, and J. Xu, Surface Science 350, 247 (1996).
24. F. Owman, P. Martensson, J. Vac. Sci. & Technol. **14**, 933 (1996).
25. H. Daimon, S. Nagano, T. Hanada, S. Ino, S.Suga, Y. Murata, Surface Science **221**, 244 (1989).
26. X. Chen, T. Abukawa, S. Kono, Surface Science **356**, 28 (1996).
27. Y. Taguchi, M. Date, N. Takagi, T. Aruga, M. Nishijima, Applied Surface Science, **82/83**, 434 (1994).
28. A. V. Zotov, E. A. Khramtsova, S. V. Ryzhkov, A. A. Saranin, A. B. Chub, V. G. Lifshits, Surface Science **316**, L1034 (1994).
29. R. Kaplan, Surface Science **215**, 111 (1989).
30. V. M. Bermudez, Applied Surface Science **84**, 45 (1995).
31. J. E. Northrup and J. Neugebauer, Phys. Rev. B **52**, R17001 (1995).
32. J. E. Northrup, Phys. Rev. Lett., 57 (1986) 154.
33. P. Badziag, Surface Science **337**, 1 (1995).

34. P. Badziag, Surface Science **352**, 396 (1996).
35. T. Abukawa, C.Y. Park, S. Kono, Surface Science **201**, L513 (1988).
36. P. Martensson, G. Meyer, N. M. Amer, E. Kaxiras, and K. C. Pandey, Phys. Rev. B **42**, 7230 (1990) .
37. B. B. Pate, Surface Science **165**, 83 (1986).
38. A. V. Hamza, G. D. Kubiak, and R. H. Stulen, Surface Science **237**, 35 (1990).
39. M. D. Allendorf, D. A. Outka, Surface Science **258**, 177 (1991).
40. S. W. King, M. C. Benjamin, R. S. Kern, J. P. Barnak, D. Hanser, R. J. Nemanich, and R. F. Davis, submitted to J. Appl. Phys.
41. Jacob van der Weide, Ph.D. dissertation, NCSU (1993).
42. S.W. King, R.J. Nemanich, and R.F. Davis, submitted to J. Electrochem. Soc.
43. S.W. King, R.J. Nemanich, and R.F. Davis, submitted to J. Electrochem. Soc.
44. C. Pirri, U. Kafader, G. Gewinner, and P. Wetzel, Solid State Comm. **89**, 313 (1994).
45. G. Gewinner, U. Kafader, P. Wetzel, and C. Pirri, J. Electron. Spect. and Rel. Phenoma.
46. J. L. Bischoff, L. Kubler, F. Lutz, M. Diani, and D. Bolmont, Solid State Comm. **83**, 823 (1992).
47. E. Puppin, C. Carbone, R. Rochow, Phys. Rev. B **46**, 13215 (1992).
48. L. Kubler, F. Lutz, J. L. Bischoff, and D. Bolmont, Surface Science **251/252**, 305 (1991).
49. S. Juillaguet, L. Kubler, M. Diani, J. L. Bischoff, G. Gewinner, P. Wetzel, N. Becourt, Surface Science **339**, 363 (1995).
50. M. Diani, J. L. Bischoff, L. Kubler, and D. Bolmont, Applied Surface Science **68**, 575 (1993).
51. O. M. Kuttel, R. G. Agostino, R. Fasel, J. Osterwalder, and L. Schlapbach, Surface Science **312**, 131 (1994).

III. Development of a System for Integrated Surface Cleaning and Oxide Formation on 6H-SiC

A. Introduction

The development of high-temperature, high-power and high-frequency devices based on SiC requires a complete understanding of the oxide formation and interface characteristics. To have SiC device technology introduced into the mainstream industrial community, it is necessary that current technologies be employed in device fabrication. Thermal oxidation of p-type SiC has led to an increase in defects that have resulted in degradation of the electrical properties. An oxide positive space charge has been estimated to be about 1.5×10^{12} cm^{-2}, and the estimation of fast interface states is of the same order [1]. It is proposed that the Al dopant on p-type SiC is more readily redistributed in SiO_2, while the N dopant on n-type is not. This yields significant quantities of Al in thermally grown oxides on p-type SiC that form Al_2O_3, which may increase the number of defects in the oxide and the SiO_2/SiC interface [2]. The resultant oxide displays an increase in space charge, a lowering of the breakdown voltage, and an increase in both fast and slow interface state densities. By using an integrated UHV system, interfaces will be prepared with lower contaminant levels , thus a better understanding of the SiC oxide formation process will be gained. The UHV compatible surface preparation and oxide formation system will be integrated with an advanced system that includes other processing and characterization capabilities that will allow for *in vacuo* characterization of the SiO_2/SiC interface followed by *ex situ* electrical characterization. From recent experiments on SiC, it was shown that the cleaning and surface preparation of SiC is a more involved process than Si [3]. In order to completely remove oxygen from the SiC surface, a Si capping layer was deposited and then thermally desorbed. This removed the oxygen within the detection limits of AES and XPS. It is unclear at this point whether or not it is necessary to totally remove all the oxygen from the SiC surface. It is proposed that the residual oxide from most surface preparation techniques is oxygen trapped at near-surface grain boundaries [4]. A systematic approach is underway to develop a process that will yield an electrical quality oxide on SiC.

B. Experimental Approach

The integrated system will allow for most of the characterization to be accomplished without exposing samples to the ambient. Furthermore, the processes will be characterized at various stages thus allowing for the understanding of the entire oxidation process. A typical process is given as follows: (1) surface preparation; (2) initial insulator formation; (3) CVD insulator deposition. A schematic of the process is shown in Fig. 1. At each of these stages, there are a wide variety techniques are available.

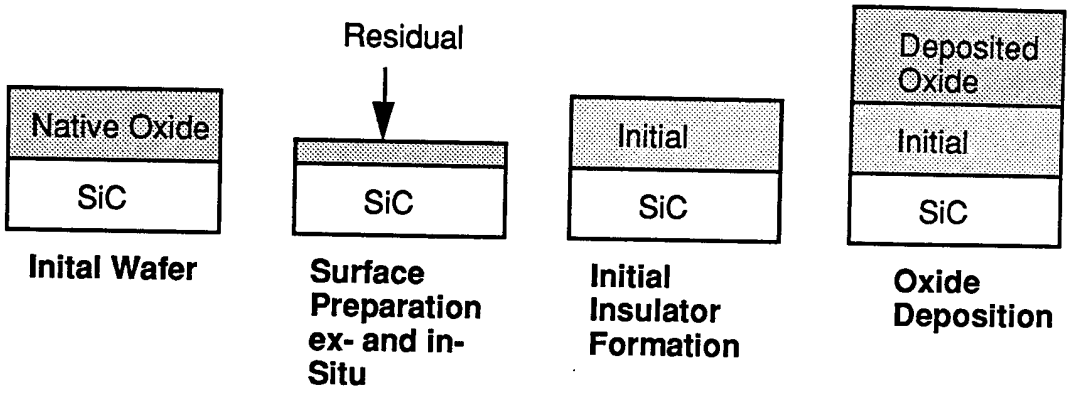

Figure 1. Basic process for insulator formation on SiC.

An experimental matrix has been set up to provide a systematic approach to the insulator formation process. Figure 2 lists the procedures and processes that will be used to determine the SiC/SiO_2 interface and deposition process. The base line procedure will be a RCA clean followed by thermal oxide growth. The base line procedure will be compared to all other procedures. *Ex situ* surface preparation will be the first process investigated. Once the *ex situ* surface preparation technique that yields the highest quality thermal oxide has been determined, it will become the standard procedure. Using the *ex situ* preparation process previously determined as a standard process, the *in situ* surface preparation will be investigated. The *in situ* process(es) that again yield the highest quality thermal oxide will be added as a standard preparation procedure. Initial insulator formation is then investigated using the previous *ex situ* and *in situ* surface preparation techniques. Once an initial insulator formation procedure that yields a higher quality oxide is determined, it will become part of the standard preparation/growth techniques. This systematic approach will investigate the various processes and chemistries that are present in the oxidation of SiC and the SiC/SiO_2 interface.

Surface preparation is arguably the most important step to high quality insulator growth. Ensuring a clean smooth surface is necessary for oxide growth. Some of the various procedures are: (1) wet chemical clean; (2) plasma cleaning; (3) HF vapor phase. Current

ex-situ	in-situ	Initial Oxide	Insulator Deposition
RCA	None	None	Thermal CVD
RCA/HF	H-Plasma	Thermal Oxidation	Plasma CVD
RCA & pH Controlled HF	H/SiH4 Plasma	Plasma Oxidation	
RCA/HF/ UV Ozone	Excess Si/ Thermal Anneal		
RCA/Nitric	[HF Vapor]		

Figure 2. Experimental matrix for high-quality insulator formation on SiC.

cleaning techniques have been developed that will yield various levels of cleaning, specifically, most procedures cannot remove all oxygen from the SiC surface. Hydrogen plasma cleaning removes surface contaminants, but, as shown in Fig. 3, leaves the residual oxide after the HF dip.

Likewise, a H/SiH_4 plasma has be shown to etch SiO_2 on Si [5] but is unable to remove the residual oxide on SiC. This is demonstrated by the Auger spectrum in Fig. 4.

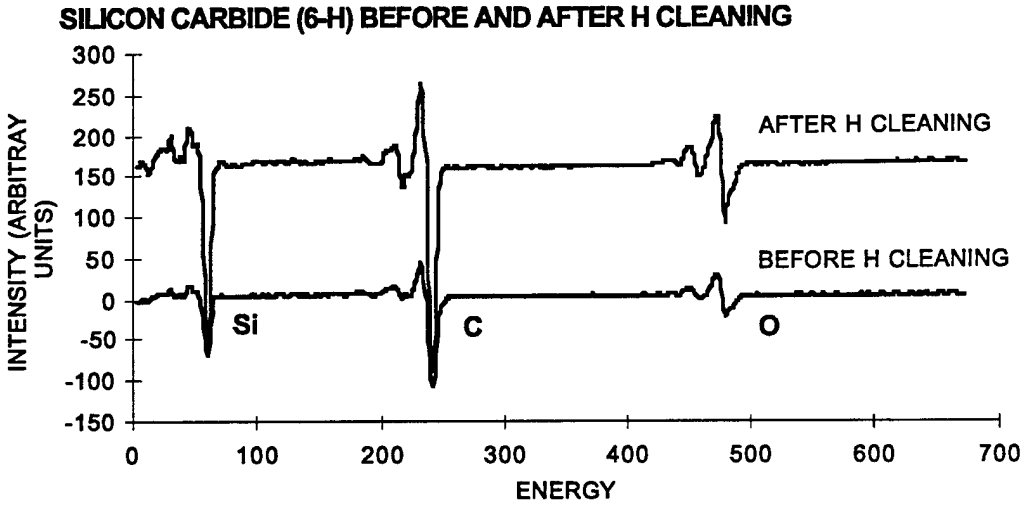

Figure 3. AES spectrum of 6-H SiC before and after H-plasma cleaning.

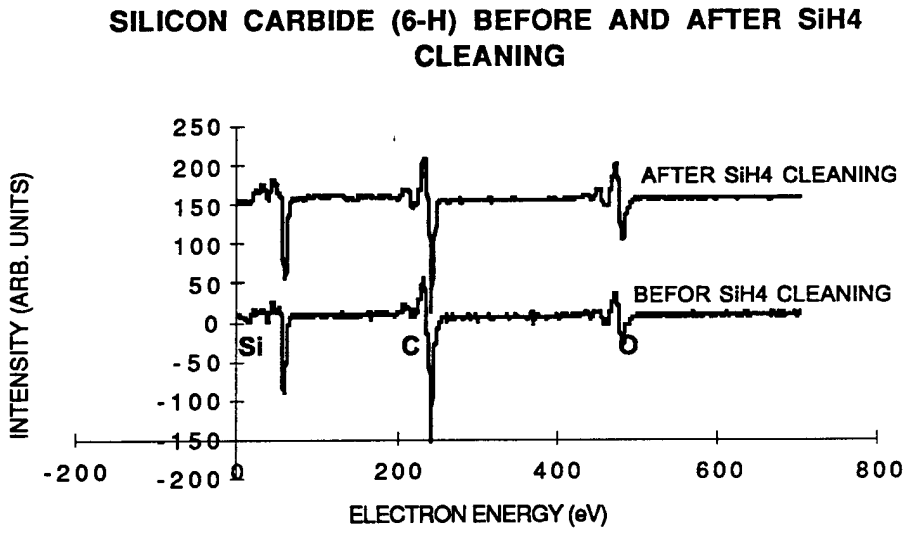

Figure 4. AES spectrum of 6-H SiC before and after H/SiH_4 plasma cleaning.

It has not been established if this residual oxide on the SiC will result in a degradation of the electrical performance of insulators grown on it. Further investigation into the effect that the residual oxide will have on electrical characteristics is needed. As shown in previous experiments [1], it is possible to remove all the oxygen contamination within detection limits.

Insulator formation on SiC is where some of the major problems are manifested. On p-type SiC, there is considerable dopant redistribution and defect formation during the transition region between SiC/SiO_2 in thermally grown oxides. By using diverse techniques for initial insulator formation and deposited oxides we will observe which process or combination of processes will minimize defect formation, dopant redistribution, and maximize the electrical properties on the initial oxide formation. Some of the procedures are: (1) UV ozone; (2) Nitric bath; (3) plasma enhanced CVD (PECVD). CVD insulator formation is the final step in the oxide formation process. Here oxide is deposited on the initial oxide to the desired thickness. This process is proposed to limit redistribution of dopants on p-type SiC. Deposited oxides do not have as desirable dielectric constants and can have considerable interface densities. By growing an initial oxidation layer, it is intended that the interface densities will be minimized, and traps will be reduced. Then by depositing an oxide on the deposited layer, it is aimed that there will be little dopant redistribution and a reduction of bulk charge and traps. Electrical characteristics will be determined. C-V and I-V measurements will be made to determine defects, such as trapped charge and interface charge. A primary goal of these experiments is to greatly increase the electrical characteristics of MOS structures in SiC. Ideally, we would be able to get the electrical characteristics close to those of Si, namely: a breakdown voltage of $\sim 1\times10^{7}$ V/cm, trap densities $\sim 10^{11}$-10^{10} cm^{-2} and interface state densities of $\sim 10^{10}$ cm^{-2}.

Currently, the oxide deposition process is be characterized for the system. Oxide deposition is one of the primary focuses of the insulator formation process. The deposited oxide qualities must be maximized before any results for SiC are obtained. Via preliminary data, the deposition rate is linear with time. Further investigation into other parameters, such as temperature and gas mixtures is needed to determine the best quality of deposited oxides. Current oxide deposition is done for Si(111) so that it maybe compared to known data. By giving a basis in silicon technology, it is thought that the transition to silicon carbide will be made more readily.

C. Conclusions

Current cleaning and surface preparation techniques for silicon may be inadequate in their current form for SiC. There is a residual oxide that remains after the currently accepted cleaning techniques which may or may not affect the electrical characteristics of deposited oxides. The integrated UHV system will be able to explore processes that have previously been

unobtainable. The uniqueness of the surface preparation integrated with the growth and characterization system allows for capabilities that have not been previously used in the characterization and growth of oxides on SiC. Currently, oxide growth is being characterized and optimized. Once the oxide deposition technique is well defined, focus will change to the initial oxidation procedure. The electrical characteristics will guide the selection of the optimal process and the surface diagnostics should allow a scientific understanding of the process.

D. Future Research Plans and Goals

Establishing a base line procedure that is equivalent to the accepted procedure for oxide growth will enable considerable focus on the examination of the oxide layers for use as gate insulators in field effect devices. The base line procedure for oxide deposition on silicon will be adapted to silicon carbide. Once the deposition of oxide on silicon carbide is well known, the interface and initial oxide formation process will be examined.

E. References

1. C. Zetterling and M. Ostling, Mat. Res. Soc. Symp. Proc. **339**, 209 (1994).
2. J. W. Palmour, R. F. Davis, H. S. Kong, S. F. Corcoran, and D. P. Griffis, J. Electrochem. Soc. **136** (2), 502 (1989).
3. R. F. Davis, M. O. Aboelfotoh, B. J. Baliga, R. J. Nemanich, M. C. Benjamin, S. W. King, M. L. O'Brien, L. S. Porter, S. Sridevan, and H. S. Tomozawa, Quarterly Technical Report, Office of Naval Research, Grant #N00014-95-1-1080, June 1996.
4. R. Kaplan and V. M. Bermudez, *Properties of Silicon Carbide*, SPEC Data Review Series, **7**, July 1992.
5. J. Barnak, N.C. State Univ. Private communication.

IV. Distribution List

Dr. Colin Wood Office of Naval Research Electronics Division, Code: 312 Ballston Tower One 800 N. Quincy Street Arlington, VA 22217-5660	3
Administrative Contracting Officer Office of Naval Research Regional Office Atlanta 101 Marietta Tower, Suite 2805 101 Marietta Street Atlanta, GA 30323-0008	1
Director, Naval Research Laboratory ATTN: Code 2627 Washington, DC 20375	1
Defense Technical Information Center 8725 John J. Kingman Road Suite 0944 Ft. Belvoir, VA 22060-6218	2